Computer simulations for the denoising effect of morphological reconstructions for CT images on hexagonal grids and regular hexagonal regions

Zheng, Xiqiang

Xiqiang Zheng, "Computer simulations for the denoising effect of morphological reconstructions for CT images on hexagonal grids and regular hexagonal regions," Proc. SPIE 12076, 2021 International Conference on Image, Video Processing, and Artificial Intelligence, 120760G (11 November 2021); doi: 10.1117/12.2611798

SPIE.

Event: Fourth International Conference on Image, Video Processing, and Artificial Intelligence (IVPAI 2021), 2021, Shanghai, China

Computer simulations for the denoising effect of morphological reconstructions for CT images on hexagonal grids and regular hexagonal regions*

Xiqiang Zheng

School of Science, Technology, Health & Human Services; Voorhees College, Denmark, SC 29042, USA
xzheng@voorhees.edu

Abstract. In this paper, morphological operations on hexagonal lattices and regular hexagonal regions are applied to 2D parallel beam computerized tomography (CT) image denoising. To show some denoising effects of the morphological operations, for an input image, we add certain amount of noise to get the noised image; and perform Radon transform and inverse Radon transform on the noised image to obtain a CT image. To compare hexagonal lattices with square lattices fairly, the CT image is resampled to an image defined on a certain randomized grid, which is in turn resampled to an image defined on a hexagonal lattice and an image defined on the corresponding square lattice (with the same sampling rate), respectively. For the morphological operations, we use a structuring element defined on a hexagonal lattice and a structuring element defined on a square lattice such that those two structuring elements have the same number of ones. Each of those two images performs an erosion with the corresponding structuring element. Then use those two images as masks and use the two corresponding eroded images as makers to perform morphological image reconstructions to obtain the two reconstructed images. Finally, both usual and Phantom images are used as test images. For many different tested noise levels, the output data show that the image reconstructed on the hexagonal lattice is usually more similar to the input image than the one reconstructed on the square lattice.

Keywords: Hexagonal lattices · morphological reconstruction · computerized tomography · image segmentation.

1 Introduction

As in [1] by Zheng, $\mathbb{R}$, $\mathbb{Z}$, $\mathbb{N}$ denote the set of real numbers, integers, and natural numbers, respectively. Let $\|\mathbf{x}\|$ denote the norm of $\mathbf{x}$ for any $\mathbf{x} \in \mathbb{R}^2$. If $\mathbf{u}, \mathbf{v} \in \mathbb{R}^2$ such that $\|\mathbf{u}\| = \|\mathbf{v}\|$ and the angle between $\mathbf{u}$ and $\mathbf{v}$ is 60° or 120°, then the set

* This research is partially supported by a Henry C. McBay faculty research fellowship from the United Negro College Fund of the USA, and a National Science Foundation grant of the USA with the Federal Award ID Number 2000158.

2021 International Conference on Image and Video Processing, and Artificial Intelligence
edited by Yudong Zhang, Proc. of SPIE Vol. 12076, 120760G
 · 0277-786X · doi: 10.1117/12.2611798

$\{k_1 \cdot \mathbf{u} + k_2 \cdot \mathbf{v} : \ k_1, k_2 \in \mathbb{Z}\}$ is called a *hexagonal lattice* generated by $\mathbf{u}$ and $\mathbf{v}$. The two numbers k_1 and k_2 are called the *affine coordinates* of the lattice point $k_1 \cdot \mathbf{u} + k_2 \cdot \mathbf{v}$. If $\|\mathbf{u}\| = \|\mathbf{v}\|$ and the angle between them is $90°$, then they generate a *square lattice*, which is a 2D *Cartesian lattice*. The usual 2D image processing is done on a square lattice for the discretization of a geometric object. However, hexagonal lattices have advantages over square lattices in some aspects. For example, in a hexagonal lattice, each lattice point has six equidistant neighbors; each Voronoi cell is well-connected to six adjacent Voronoi cells.

If $\|\mathbf{u}\| = \|\mathbf{v}\|$ and the angle between $\mathbf{u}$ and $\mathbf{v}$ is $120°$, then for each $n \in \mathbb{N}$ let

$$\Xi_n = \{k_1 \cdot \mathbf{u} + k_2 \cdot \mathbf{v} : \ k_1, k_2 \in \mathbb{Z}, |k_1| \leq n, |k_2| \leq n, |k_1 - k_2| \leq n\}.$$

As in [2, 3] by Zheng, Ξ_n is called a *regular hexagonal structure* (RHS) with parameter n. Fig. 1 in [2] shows the geometric structures of Ξ_3. Ξ_n is actually a discretization of a regular hexagonal region. As pointed out by Zheng and Gu at Section 6 in [4], the domain of a 2D computerized tomography (CT) image may be assumed to be circular because of rotations of CT machines. In some situations, the 2D region to be scanned may be embedded into a regular hexagonal region more compactly than the corresponding square region. Hence 2D CT image reconstruction on Ξ_n may produce a smaller set of data and better image quality than the usual image reconstruction on a square region. Furthermore, as shown in [2] by Zheng or in [5] by Li, regular hexagonal structures allow efficient pixel indexing and storage schemes for image processing on hexagonal lattices. Because morphological operations are important tools for image processing, in this paper, we perform computer simulations to show certain denoising effects of morphological reconstruction for CT images defined on RHSs.

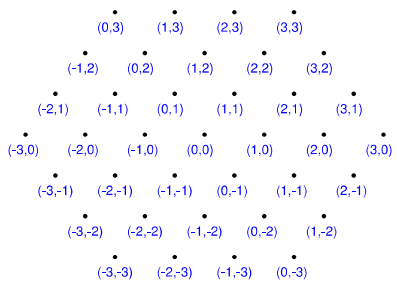

Fig. 1. The lattice points of Ξ_3 and their affine coordinates.

2 Morphological Operations on Regular Hexagonal Structures

Morphological operations on the usual Cartesian lattices can be found in references such as [6] by Serra, [7] by Shih, [8] by Bartovsky et al., and [9] by Bartovsky. They are important in some image processing tasks such as filtering and segmentation. In [2], Zheng defined morphological operations for images defined on RHSs and provided some efficient computational algorithms for the computation of dilations and erosions. Let us review some of those definitions in the following.

For each integer $m > 0$, a binary image defined on the RHS Ξ_m is just an indicator function b on a subset of S of Ξ_m, i.e., $b(s) = 1$ for each $s \in S$ and $b(s) = 0$ for each $s \notin S$. Hence, the binary image can be just denoted as S. For any $m, n \in \mathbb{N}$, the *dilation* and *erosion* of the binary image Ξ_m by the structuring element Ξ_n are denoted as $\Xi_m \bigoplus \Xi_n$ and $\Xi_m \Theta \Xi_n$, respectively. Thus, $\Xi_m \bigoplus \Xi_n = \{\mathbf{p} + \mathbf{q} : \ \mathbf{p} \in \Xi_m, \mathbf{q} \in \Xi_n\}$ and

$$\Xi_m \Theta \Xi_n = \{\mathbf{p} \in \Xi_m : \ \mathbf{p} + \mathbf{q} \in \Xi_m \ for \ each \ \mathbf{q} \in \Xi_n\}.$$

Let f be a greyscale image defined on Ξ_m. The *greyscale dilation* and *greyscale erosion* of f by the structuring element Ξ_n are defined to be $[\delta_{\Xi_n}(f)](\mathbf{p}) := max\{f(\mathbf{p} + \mathbf{q}) : \ \mathbf{q} \in \Xi_n\}$ and $[\varepsilon_{\Xi_n}(f)](\mathbf{p}) := min\{f(\mathbf{p} - \mathbf{q}) : \ \mathbf{q} \in \Xi_n\}$ for each $\mathbf{p} \in \Xi_m$, respectively. Efficient algorithms for the computation of $[\delta_{\Xi_n}(f)]$ and $[\varepsilon_{\Xi_n}(f)]$ are shown in [2] by Zheng.

3 Morphological Reconstruction for Hexagonal CT Images and Certain Denoising Effects

The concept of morphological image reconstruction for Cartesian lattices can be found in references such as [10] by Vincent, [11] by Ledda, [12] by Vartak and Mankar, and [13] by Chudasama et al. Given two images M and N such that $M \geq N$ (by elementwise comparisons), the morphological reconstruction is the process of dilations from N under M until idempotence. The morphologically idempotent image from the dilations is called the *morphologically reconstructed image*. The two images M and N are called the *mask* and the *marker* of the reconstruction, respectively. In this section, we show some procedures and certain denoising effects for the morphological operations on RHSs versus square lattices for CT images.

Let SE_4 be the structuring element represented by the matrix

$$SE_4 = \begin{bmatrix} 0\,0\,1\,1\,1\,0\,0 \\ 0\,1\,1\,1\,1\,1\,0 \\ 1\,1\,1\,1\,1\,1\,1 \\ 1\,1\,1\,1\,1\,1\,1 \\ 1\,1\,1\,1\,1\,1\,1 \\ 0\,1\,1\,1\,1\,1\,0 \\ 0\,0\,1\,1\,1\,0\,0 \end{bmatrix}.$$

To fairly compare hexagonal lattices with square lattices for morphological reconstruction, we use Ξ_3 as the structuring element for hexagonal lattices because both SE_4 and the indicator function of Ξ_3 (as shown in Fig. 1) have 37 ones.

Let $s = \sqrt{\frac{2}{\sqrt{3}}}$, $\mathbf{u} = s \cdot [1, 0]$, $\mathbf{v} = s \cdot \left[-\frac{1}{2}, \frac{\sqrt{3}}{2}\right]$, and let Ω be the hexagonal lattice generated by $\mathbf{u}$ and $\mathbf{v}$. Obviously the angle between $\mathbf{u}$ and $\mathbf{v}$ is 120°, and the area of the Voronoi cells of Ω is 1. Hence the hexagonal lattice Ω and the Cartesian lattice $\mathbb{Z}^2$ have the same sampling rate on the 2D space $\mathbb{R}^2$.

In Matlab, a usual image is defined on a square lattice and is represented by a matrix $M = (m_{i,j})$, where $m_{i,j}$ denotes the image value at the coordinate $[j, i]$ whose x coordinate is j and y coordinate is i. To perform the resampling among the square lattices, the corresponding hexagonal lattices, and certain random grids for images represented by matrices, we need the following notations. For any $n \in \mathbb{N}$, let $r = \frac{n-1}{2}$, $C_r = \left\{[x, y] \in \mathbb{R}^2 : \ x^2 + y^2 \leq r^2\right\}$, $J_c = \left\{x - \frac{n+1}{2} : \ x \in \mathbb{N} \ and \ 1 \leq x \leq n\right\}$, $(J_c)^2 = \{[x, y] : \ x \in J_c \ and \ \ y \in J_c\}$, and $P = (J_c)^2 \bigcap C_r$. Then let $m = \left\lceil \frac{k \cdot r}{s} \right\rceil$ and $Q = \Xi_m \bigcap C_r$. Let $A_{s,Cir}$, $B_{s,Cir}$, $A_{s,Cir,Rand}$, and $B_{s,Cir,Rand}$ be the 1D vectors having the same length L_s such that

$$P = \{[A_{s,Cir}(i), B_{s,Cir}(i)] : \ 1 \leq i \leq L_s\},$$

$$A_{s,Cir,Rand}(i) = A_{s,Cir}(i) + 0.98 \cdot (rand - 0.5)$$

where *rand* is the command (as in Matlab) generating a random number between 0 and 1, and

$$B_{s,Cir,Rand}(i) = B_{s,Cir}(i) + 0.98 \cdot (rand - 0.5).$$

Also let $A_{h,Cir}$, $B_{h,Cir}$, $A_{h,Cir,Rand}$, and $B_{h,Cir,Rand}$ be the 1D vectors having the same length L_h such that

$$Q = \{[A_{h,Cir}(i), B_{h,Cir}(i)] : \ 1 \leq i \leq L_h\},$$

$$A_{h,Cir,Rand}(i) = A_{h,Cir}(i) + 0.98 \cdot (rand - 0.5),$$

and $B_{h,Cir,Rand}(i) = B_{h,Cir}(i) + 0.98 \cdot (rand - 0.5)$. Now we apply the steps in the following Algorithm 1 to show certain denoising effects of morphological reconstructions on RHSs for 2D CT images.

Algorithm 1: The denoising effects for morphological reconstruction on square lattices versus hexagonal lattices.
Input: A greyscale image M, which is resampled to the size 1024 by 1024.
Output: The dissimilarity measures for morphological reconstruction on the square lattice $\mathbb{Z}^2$ versus the hexagonal lattice Ω.
1) Because we need to use SE_4 and Ξ_3 as structuring elements, the size of images should not be small. For any rectangular 2D Cartesian image (in greyscale), resize it to a 1024 by 1024 image; and denote the resized image as I_0.
2) Add certain amount of noise to I_0, and denote the noised image as I_1. For example, we can add *Salt & Pepper* noise or *Gaussian* noise to I_0.
3) Let $\Theta = \{0°, 1°, 2°, ..., 179°\}$ and perform Radon transform on I_1 with directions specified by angles in Θ to get the sinogram.

4) Let the output image size be the same as the size of I_1; and apply the inverse Radon transform on the sinogram with the *linear* interpolation method, *Ram-Lak* filter, and angles in Θ to obtain the output image I_2.

5) Let $r = \frac{n-1}{2}$, and let X_r and Y_r be two n by n matrices such that each row of X_r is equal to J_c and each column of Y_r is equal to the transpose of J_c. To fairly compare hexagonal lattices with square lattices for morphological operations, we resample the two images I_0 and I_2 (defined on the coordinates specified by X_r and Y_r) into the two images $I_{0,rand,Cir}$ and $I_{2,rand,Cir}$ (defined on the coordinates specified by $A_{s,Cir,Rand}$ and $B_{s,Cir,Rand}$) respectively, where $A_{s,Cir,Rand}$ and $B_{s,Cir,Rand}$ are defined before and represent the corresponding sets of x and y coordinates of $P := (J_c)^2 \bigcap C_r$. For example, in Matlab, the resampling processes can be done as the following.

$$I_{0,rand,Cir} = griddata\,(X_r(:), Y_r(:), I_0(:), B_{s,Cir,Rand}, A_{s,Cir,Rand}, 'linear')\,;$$
$$I_{2,rand,Cir} = griddata\,(X_r(:), Y_r(:), I_2(:), B_{s,Cir,Rand}, A_{s,Cir,Rand}, 'linear')\,.$$

6) Let $A_{h,Cir}$ and $B_{h,Cir}$ be as defined before and represent the corresponding sets of x and y coordinates of $Q := \Xi_m \bigcap C_r$, respectively. So are $A_{s,Cir}$ and $B_{s,Cir}$ for P. We resample the image $I_{0,rand,Cir}$ into the two images S_{Cir} (defined on the coordinates specified by $B_{s,Cir}$ and $A_{s,Cir}$) and H_{Cir} (defined on the coordinates specified by $B_{h,Cir}$ and $A_{h,Cir}$). We also resample the image $I_{2,rand,Cir}$ into the two images $S_{Cir,Noised}$ (defined on the coordinates specified by $B_{s,Cir}$ and $A_{s,Cir}$) and $H_{Cir,Noised}$ (defined on the coordinates specified by $B_{h,Cir}$ and $A_{h,Cir}$), respectively. In Matlab, the resampling processes can be done as the following.

$$F_{Rand} = scatterInterpolant\,(B_{s,Cir}, A_{s,Cir}, I_{0,Rand,Cir}, 'linear', 'none')\,;$$
$$F_{Noised,Rand} = scatterInterpolant\,(B_{s,Cir}, A_{s,Cir}, I_{2,Rand,Cir}, 'linear', 'none')\,;$$
$$S_{Cir} = F_{Rand}\,(B_{s,Cir}, A_{s,Cir})\,; S_{Cir,Noised} = F_{Rand,Noised}\,(B_{s,Cir}, A_{s,Cir})\,;$$
$$H_{Cir} = F_{Rand}\,(B_{h,Cir}, A_{h,Cir})\,; H_{Cir,Noised} = F_{Rand,Noised}\,(B_{h,Cir}, A_{h,Cir})\,.$$

7) Using zero paddings, extend $S_{Cir,Noised}$ to S_{Noised} that is defined on $(J_c)^2$; and extend $H_{Cir,Noised}$ to H_{Noised} that is defined on Ξ_m.

8) Let $S_{Noised,Eroded}$ be the morphologically eroded image from S_{Noised} using the structuring element SE_4, and let $H_{Noised,Eroded}$ be the eroded image from H_{Noised} using the structuring element Ξ_3 on the hexagonal lattice Ω.

9) Let R_s be the morphologically reconstructed image using $S_{Noised,Eroded}$ as the marker and S_{Noised} as the mask; and let R_h be the reconstructed image on the hexagonal lattice Ω using $H_{Noised,Eroded}$ as the marker and H_{Noised} as the mask.

10) Let $R_{s,Cir}$ and $R_{h,Cir}$ be the 1D vectors corresponding to R_s and R_h restricted to the circular region C_r, respectively.

11) Finally compute the dissimilarity measures between $R_{s,Cir}$ and S_{Cir}, and the dissimilarity measures between $R_{h,Cir}$ and H_{Cir} based on the L_1 and L_2 norms, which are used in [14] by Kim et al. and in [15] by Nourian and Aahmadzadeh, respectively. In Matlab, the code can be

$$dfL1_{S,Rs} = norm\,(S_{Cir} - R_{s,Cir}, 1)\,; dfL1_{H,Rh} = norm\,(H_{Cir} - R_{h,Cir}, 1)\,;$$
$$dfL2_{S,Rs} = norm\,(S_{Cir} - R_{s,Cir}, 2)\,; dfL2_{H,Rh} = norm\,(H_{Cir} - R_{h,Cir}, 2).$$

We also computed several dissimilarity measures discussed in [16] by Goshtasby including Pearson correlation coefficient, Tanimoto measure, minimum ratio, and intensity ratio variance. Let F and G be two images of the same size; and assume that F and G are represented by 1D column vectors of length L. The *Tanimoto measure* between F and G is denoted as $T_M(F,G)$ and defined by $T_M(F,G) := \frac{F^t \cdot G}{\|F-G\|^2 + F^t \cdot G}$. The *Pearson correlation coefficient* is usually called *correlation coefficient*.

Let F_i and G_i be the *ith* component of F and G. For each integer i with $1 \leq i \leq L$, if $F_i = G_i$, let $r_i = 1$; otherwise, let $r_i = 0$ if $F_i \cdot G_i = 0$ and let $r_i = min\left\{\frac{F_i}{G_i}, \frac{G_i}{F_i}\right\}$ if $F_i \cdot G_i \neq 0$. The *minimum ratio* between F and G is denoted as $M_R(F,G)$ and defined by $M_R(F,G) := \frac{1}{L}\sum_{i=1}^{L} r_i$.

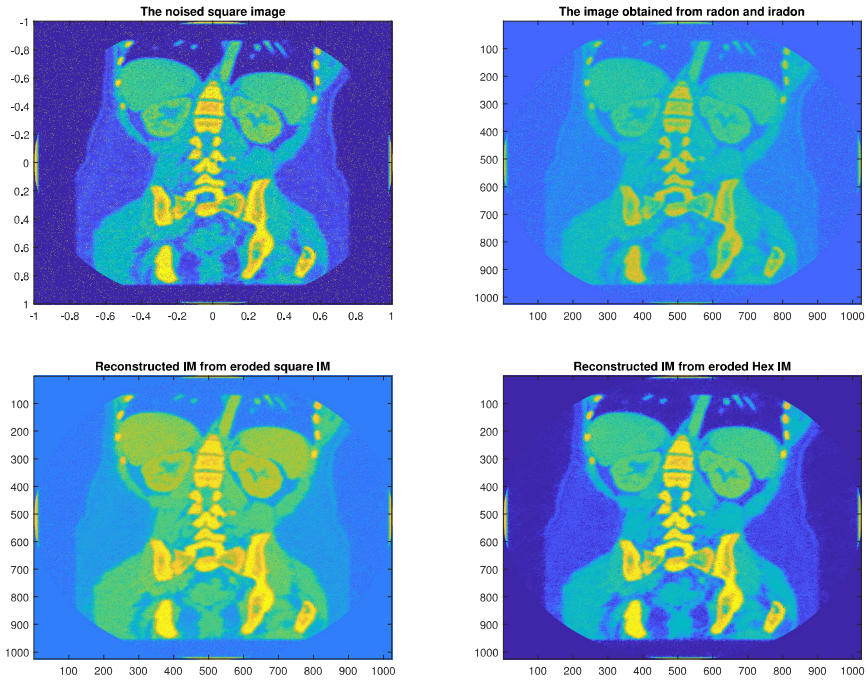

Fig. 2. Test of Algorithm 1 using an abdominal CT scan image and salt & pepper noise with density 0.05. The top left is the original noised image; the top right is the output image after Radon and inverse Radon transforms; the bottom left shows the morphologically reconstructed image using the square lattice; and the bottom right shows the morphologically reconstructed image using the hexagonal lattice.

Let ε be a small positive number (in our computations we let $\varepsilon = 10^{-8}$). If F or G have negative components, then let ε be the difference between 10^{-8} and the minimal component. Finally let $r_i = \frac{F_i + \varepsilon}{G_i + \varepsilon}$ for each integer i with $1 \leq i \leq L$.

Table 1. Using an abdominal CT scan image as the input of Algorithm 1 and using salt & pepper noise with density 0.05 in Fig 2, this table shows the corresponding dissimilarity measures between P_{Cir} and Q_{Cir} that denote the original and the morphologically reconstructed images restricted to the circular region respectively, where the last row is the dissimilarity measures for the hexagonal lattice.

Dissimilarity Measures	L_1 Norm	L_2 Norm	$intRatioV$	$PeCorr$	$TanM$	$minRatio$
$d(S_{Cir}, R_{s,Cir})$	$8.658 \cdot 10^6$	$1.333 \cdot 10^4$	$5.679 \cdot 10^{15}$	0.971	0.981	0.785
$d(H_{Cir}, R_{h,Cir})$	$8.077 \cdot 10^6$	$1.273 \cdot 10^4$	$2.910 \cdot 10^{15}$	0.974	0.983	0.795

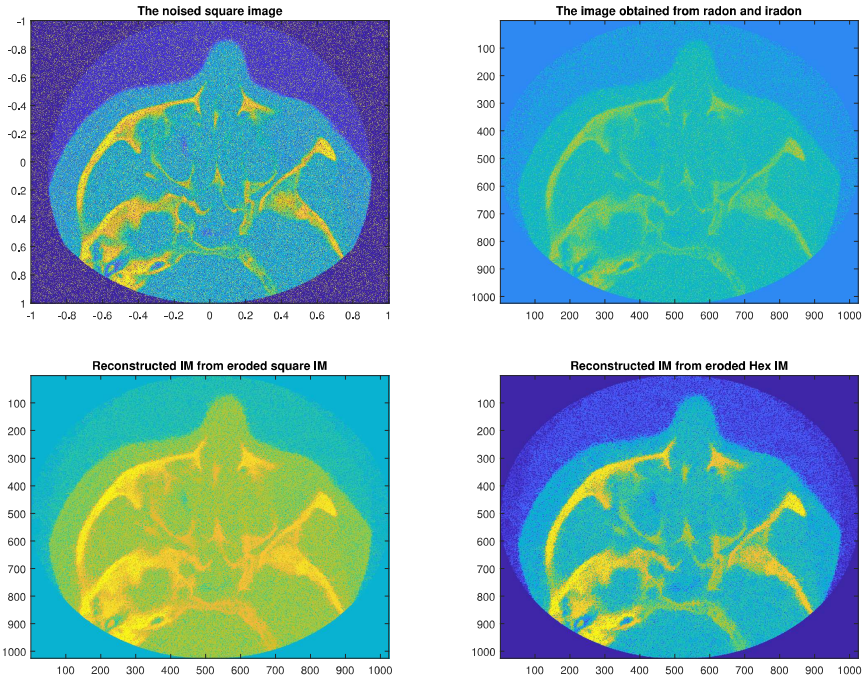

Fig. 3. Test of Algorithm 1 using a usual image and salt & pepper noise with density 0.20. The top left is the original noised image; the top right is the output image after Radon and inverse Radon transforms; the bottom left shows the morphologically reconstructed image using the square lattice; and the bottom right shows the morphologically reconstructed image using the hexagonal lattice.

Table 2. The dissimilarity measures between P_{Cir} and Q_{Cir} when the salt & pepper with density 0.2 as in Fig 3, where P_{Cir} and Q_{Cir} mean the same as Table 1.

Dissimilarity Measures	L_1 Norm	L_2 Norm	$intRatioV$	$PeCorr$	$TanM$	$minRatio$
$d(S_{Cir}, R_{s,Cir})$	$1.7918 \cdot 10^7$	$2.6152 \cdot 10^4$	$2.0636 \cdot 10^{16}$	0.8754	0.9278	0.6858
$d(H_{Cir}, R_{h,Cir})$	$1.6728 \cdot 10^7$	$2.4911 \cdot 10^4$	$1.6377 \cdot 10^{16}$	0.8897	0.9337	0.6977

The *intensity-ratio variance* from F to G is denoted as $R_v(F,G)$ and defined by $R_v(F,G) := \frac{1}{L}\Sigma_{i=1}^{L}(r_i - \bar{r})^2$; the *intensity-ratio variance* between F and G is denoted as $I_v(F,G)$ and defined by $I_v(F,G) := \frac{1}{2}(R_v(F,G) + R_v(G,F))$.

We tested Algorithm 1 using two different CT images and a Phantom image with three different kinds of noise. The input image of Algorithm 1 for Fig. 2 and Table 1 is an abdominal CT scan image downloaded from the link of CT scans in the website sansumclinic.org; and the input for Fig. 3 and Table 2 is a 2D CT scan image downloaded from a blog link of the website sinuswellbeing.com. In Step 2 of Algorithm 1, *salt & pepper* noise is added (in Step 2 of Algorithm 1) with noise density 0.05 and 0.2 to generate Figs. 1 and 2, respectively. Fig. 2 shows the noised image, the image after Radon and inverse Radon transforms, the morphologically reconstructed image using the square lattice, and the morphologically reconstructed image using the hexagonal lattice. Let intRatioV, PeCorr, TanM, and minRatio denote the intensity-ratio variance, Pearson correlation coefficient, Tanimoto measure, and minimum ratio, respectively. Table 1 shows the results of the six dissimilarity measures that we have introduced. Smaller values for the dissimilarity measures in terms of L_1 norm, L_2 norm, and intensity-ratio variance imply that F and G are more similar, but bigger values for the dissimilarity measures in terms of Pearson correlation coefficient, Tanimoto measure, and minimum ratio imply that F and G are more similar.

When the *salt & pepper* noise density is increased to 0.2 from 0.05, the corresponding results are shown in Fig. 3 and Table 2. When the usual image is replaced by the 1024 by 1024 Phantom image with *salt & pepper* noise at density 0.05, the corresponding results are shown in Fig. 4 and Table 3. We also tested Algorithm 1 using a Phantom image with Gaussian noise as well as an abdominal CT scan image with Poisson noise; and the results are shown in Figs. 5 and 6 along with Tables 4 and 5.

Table 3. The dissimilarity measures between P_{Cir} and Q_{Cir} when a Phantom image is used as the input of Algorithm 1 and when the salt & pepper noise with density 0.05 is applied as in Fig 4, where P_{Cir} and Q_{Cir} mean the same as Table 1.

Dissimilarity Measures	L_1 Norm	L_2 Norm	$intRatioV$	$PeCorr$	$TanM$	$minRatio$
$d(S_{Cir}, R_{s,Cir})$	$3.498 \cdot 10^4$	53.8100	$1.556 \cdot 10^{11}$	0.9673	0.9525	0.4495
$d(H_{Cir}, R_{h,Cir})$	$3.155 \cdot 10^4$	50.8512	$1.347 \cdot 10^{11}$	0.9719	0.9571	0.4612

4 Summary

We have developed an algorithm to show certain denoising effects of morphological image reconstruction on hexagonal versus square lattices, and tested the algorithm using both CT and Phantom images with three different kinds of noise. As shown in the figures, the morphologically reconstructed image using

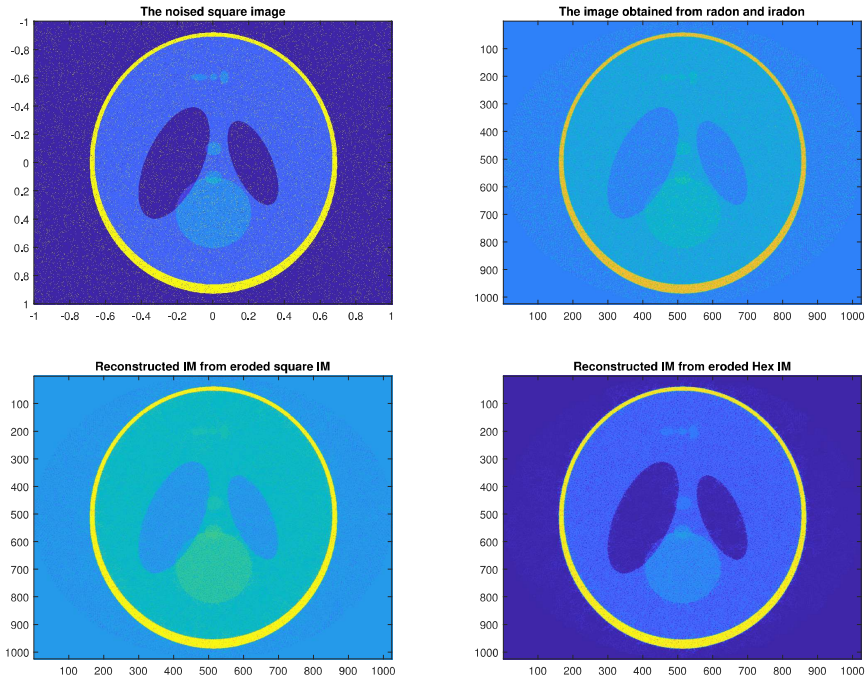

Fig. 4. Test of Algorithm 1 using a Phantom image and salt & pepper noise with density 0.05. The top left is the original noised Phantom image; the top right is the output image after Radon and inverse Radon transforms; the bottom left shows the morphologically reconstructed image using the square lattice; and the bottom right shows the morphologically reconstructed image using the hexagonal lattice.

Table 4. The dissimilarity measures between P_{Cir} and Q_{Cir} when the input of Algorithm 1 is a Phantom image and when Gaussian noise is added as in Fig 5, where P_{Cir} and Q_{Cir} mean the same as Table 1.

Dissimilarity Measures	L_1 Norm	L_2 Norm	$intRatioV$	$PeCorr$	$TanM$	$minRatio$
$d(S_{Cir}, R_{s,Cir})$	$2.7494 \cdot 10^4$	39.7424	$4.9319 \cdot 10^{10}$	0.9842	0.9736	0.4777
$d(H_{Cir}, R_{h,Cir})$	$2.5685 \cdot 10^4$	37.9757	$2.3873 \cdot 10^{10}$	0.9859	0.9758	0.4820

Table 5. The dissimilarity measures between P_{Cir} and Q_{Cir} when the input of Algorithm 1 is an abdominal CT scan image and when Poisson noise is added as in Fig 6, where P_{Cir} and Q_{Cir} mean the same as Table 1.

Dissimilarity Measures	L_1 Norm	L_2 Norm	$intRatioV$	$PeCorr$	$TanM$	$minRatio$
$d(S_{Cir}, R_{s,Cir})$	$3.1031 \cdot 10^6$	4878.3	$2.8735 \cdot 10^{12}$	0.9972	0.9973	0.7458
$d(H_{Cir}, R_{h,Cir})$	$3.0063 \cdot 10^6$	4785.7	$2.3756 \cdot 10^{12}$	0.9974	0.9974	0.7525

the hexagonal lattice visually is usually better than the one using the corre-

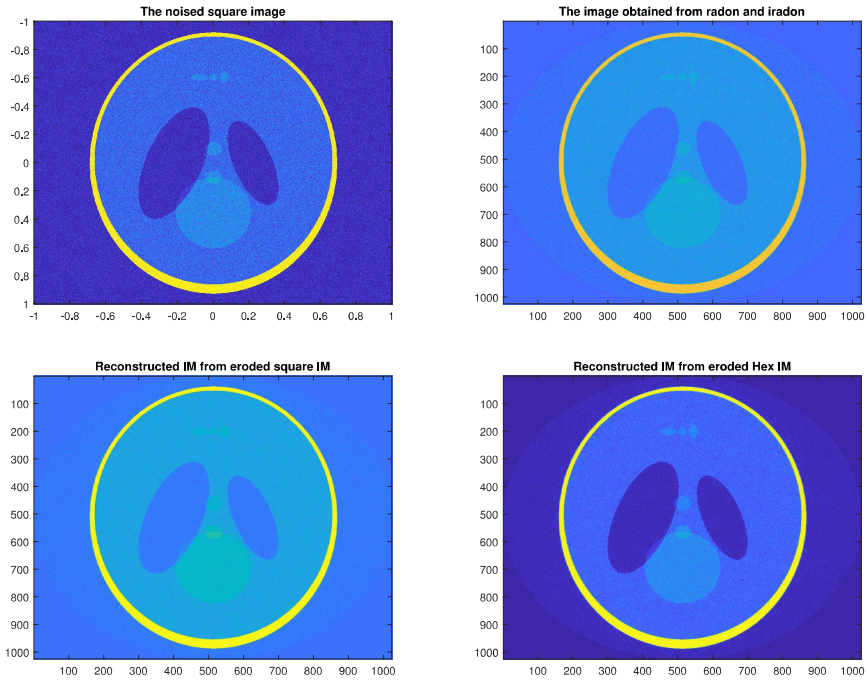

Fig. 5. Test of Algorithm 1 using a Phantom image and Gaussian noise. The top left is the original noised Phantom image; the top right is the output image after Radon and inverse Radon transforms; the bottom left shows the morphologically reconstructed image using the square lattice; and the bottom right shows the morphologically reconstructed image using the hexagonal lattice.

sponding square lattice. We also computed several usual dissimilarity measures. As shown in the tables, for the hexagonal lattice, the L_1 norm, L_2 norm, and the intensity-ratio variance are smaller; the Pearson correlation coefficient, Tanimoto measure, and minimum ratio are bigger. All values in the tables imply that, the image reconstructed on the hexagonal lattice Ω is usually more similar to the input image (before adding noise) than the one reconstructed on the corresponding square lattice $\mathbb{Z}^2$; hence the morphological image reconstruction effect for the hexagonal lattice is better than or almost the same as the effect for the corresponding square lattice. Especially, the hexagonal lattice exhibits very good denoising effects for salt & pepper noise and Gaussian noise. We performed the experiments for many times; the experimental results are usually consistent.

As mentioned in the introduction, the 2D region to be scanned may be embedded into a regular hexagon more tightly than into a square. A RHS provides a good discretization of a regular hexagon. As shown in [17] by Knaup et el., and [18] by Mueller and Xu, CT image reconstruction from sinograms using hexagonal lattices is more effective than the reconstruction using the corresponding

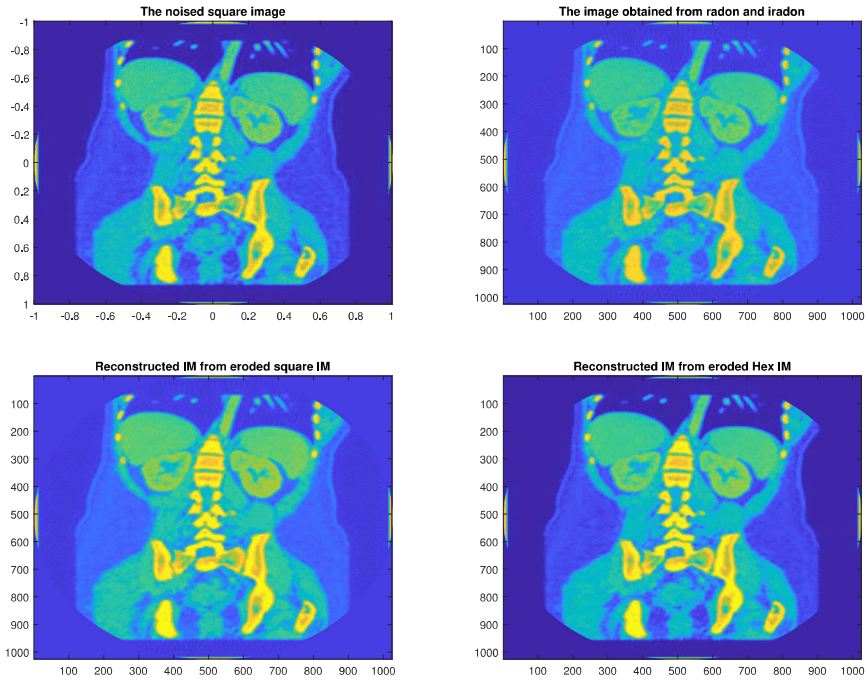

Fig. 6. Test of Algorithm 1 using an abdominal CT scan image and Poisson noise. The top left is the original noised Phantom image; the top right is the output image after Radon and inverse Radon transforms; the bottom left shows the morphologically reconstructed image using the square lattice; and the bottom right shows the morphologically reconstructed image using the hexagonal lattice.

square lattices. During the actual CT image formation, we may reconstruct CT images on both hexagonal and square lattices from the same sinogram as usual, and perform image processing on the two different kinds of lattices, respectively. Because the advantages of hexagonal lattices, the reconstructed image on the hexagonal lattice may be beneficial for some tasks such as image deniosing or segmentation. Therefore, CT image reconstruction (from sinograms) and the morphological reconstruction using RHSs may be applied to CT imaging. The success of the 2D situation can usually be generalized to 3D, and the 3D situation may achieve better effects. In the future, we may develop efficient algorithms for image reconstruction and morphological operations on 3D optimal sampling lattices and efficient domains as in [4] or develop the corresponding algorithms for modern helical CT.

References

1. Zheng, X.: Rectangular body-centered cuboid packing lattices and their possible applications. Journal of Computer Science Research **1**(2), 1–7 (2019).
2. Zheng, X.: Some efficient algorithms for morphological operations on hexagonal lattices and regular hexagonal domains. SPIE Proceedings **11584**, 115840B-1–9, (2020).
3. Zheng, X.: Efficient Fourier transforms on hexagonal arrays. (Ph D. Thesis) University of Florida, 1–140 (2007).
4. Zheng, X., Gu, F.: Fast Fourier transform on FCC and BCC lattices with outputs on FCC and BCC lattices respectively. J. Math. Imaging Vis. **49**(3), 530–550 (2014).
5. Li, X.: Storage and addressing scheme for practical hexagonal image processing. Journal of Electronic Imaging **22**(1), 1–3 (2013).
6. Serra, J.: Image analysis and mathematical morphology. Academic Press, London (1982).
7. Shih, F.: Image Processing and Mathematical Morphology: Fundamentals and Applications. 1st edn. CRC Press (2017).
8. Bartovsky, J., Dokladalova, E., Dokladal, P., Georgiev, V.: Pipeline architecture for compound morphological operators. IEEE International Conference on Image Processing, 3765–3768 (2010).
9. Bartovsky, J.: Hardware architectures for morphological filters with large structuring elements. (Ph D. Thesis) University of Paris-Est, 1–94 (2012).
10. Vincent, L.: Morphological grayscale reconstruction in image analysis: applications and efficient algorithms. IEEE Transactions on Image Processing **2**(2), 176–201, (1993).
11. Ledda, A.: Mathematical Morphology in Image Processing. (Ph D. Thesis) Ghent University, 1–290 (2007).
12. Vartak, A. P., Mankar, V.: Morphological Image Segmentation Analysis. International Journal of Computer Science and Applications **6**(2), 0974–1011 (2013).
13. Chudasama, D., Patel, T., Joshi, S., Prajapati, G.I.: Image Segmentation using Morphological Operations. Int. J. Comput. Appl. **117**(2), 16–19 (2015).
14. Kim, J., Glide-Hurst, C., Doemer, A., Wen, N., Movsas, B., Chetty, I. J.: Implementation of a novel algorithm for generating synthetic CT images from magnetic resonance imaging data sets for prostate cancer radiation therapy. Int. J. Radiat. Oncol. Biol. Phys. **91**(1), 39–47 (2015).
15. Nourian, M. B., Aahmadzadeh, M. R.: Image de-noising with virtual hexagonal image structure. 1st Iranian Conference on Pattern Recognition and Image Analysis (PRIA), (2013).
16. Goshtasby, A.A.: Similarity and Dissimilarity Measures. In: Image Registration: Principles, Tools and Methods, Springer, 224–239 (2012).
17. Knaup, M., Steckmann, S., Bockenbach, O., Kachelriess, M.: Image reconstruction using hexagonal grids. In: IEEE Nuclear Science Symposium Conf. Record, 3074–3076 (2007).
18. Mueller, K, Xu, F.: Optimal Sampling Lattices for High-Fidelity CT Reconstruction. In: IEEE Medical Imaging Conference Record, Orlando, FL, 1–5 (2009).